Journal of Applied Physics

Understanding the mechanism of hardness enhancement in tantalum-substituted tungsten monoboride solid solutions

Cite as: J. Appl. Phys. **125**, 082529 (2019); https://doi.org/10.1063/1.5054616
Submitted: 31 August 2018 . Accepted: 22 December 2018 . Published Online: 14 January 2019

Jialin Lei, Michael T. Yeung, Reza Mohammadi, Christopher L. Turner, Jinyuan Yan, Richard B. Kaner, and Sarah H. Tolbert

Journal of Applied Physics ARTICLE scitation.org/journal/jap

Understanding the mechanism of hardness enhancement in tantalum-substituted tungsten monoboride solid solutions

Cite as: J. Appl. Phys. **125**, 082529 (2019); doi: 10.1063/1.5054616
Submitted: 31 August 2018 · Accepted: 22 December 2018 ·
Published Online: 14 January 2019

Jialin Lei,[1] Michael T. Yeung,[1] Reza Mohammadi,[1,2] Christopher L. Turner,[1] Jinyuan Yan,[3] Richard B. Kaner,[1,4,5,a)] and Sarah H. Tolbert[1,4,5,a)]

AFFILIATIONS

[1]Department of Chemistry and Biochemistry, University of California, Los Angeles, California 90095, USA
[2]Department of Mechanical and Nuclear Engineering, Virginia Commonwealth University, Richmond, Virginia 23284, USA
[3]Advanced Light Source, Lawrence Berkeley National Laboratory, Berkeley, California 94720, USA
[4]Department of Materials Science and Engineering, University of California, Los Angeles, California 90095, USA
[5]California NanoSystems Institute (CNSI), University of California, Los Angeles, California 90095, USA

[a)]**Authors to whom correspondence should be addressed:** tolbert@chem.ucla.edu and kaner@chem.ucla.edu

ABSTRACT

The differential strain behavior of $Ta_xW_{1-x}B$ solid solutions has been studied as a function of composition using high-pressure radial X-ray diffraction in a diamond-anvil cell under non-hydrostatic pressure (up to ~65 GPa) to understand the hardening mechanisms in this family of materials. The hardness of tungsten monoboride (WB) can be increased by adding tantalum and reaches a maximum at a doping level of 50 at. % with a value of 42.8 ± 2.6 GPa under an applied load of 0.49 N. Plateaus were observed in the differential strain data for both the (020) and (002) directions, suggesting that this is the primary slip system in this material. These plateaus were modified by the addition of Ta, indicating that strengthening of the (002) and (020) planes by solid solution hardening was primarily responsible for the hardness enhancements in $Ta_xW_{1-x}B$ solid solutions. In contrast, the differential strain supported by the (200) plane linearly increases with pressure up to the highest pressures reached in this work (>60 GPa) and shows almost no change with metal composition. Because of the very different compression behavior in the (200) and (020) planes, change in the b/a ratio with pressure provides a unique way to visualize the onset of plastic behavior. This onset varies from ~15 GPa for samples with 5% Ta to more than 30 GPa for the sample with 50% Ta. In addition, the ambient bulk modulus of each solid-solution sample was determined using the second-order Birch-Murnaghan equation-of-state and found to be ~340 GPa for all phases.

INTRODUCTION

Attempts to meet the increasing demand for high-performance and long-lasting abrasives, cutting tools, and forming dies have resulted in the development of superhard materials (Vicker's hardness ≥40 GPa). While diamond and cubic boron nitride (c-BN) are the most important superhard abrasives, materials that can be synthesized without the need for high pressure are more desirable. Tungsten tetraboride (WB_4), therefore, has triggered a great deal of interest among researchers because of its desirable mechanical properties such as high Vickers hardness (43.3 ± 2.9 GPa)[1,2] and high incompressibility (324 ± 3 GPa).[3] The synthesis of WB_4 requires neither high pressures like c-BN and diamond nor expensive platinum group metal found in other superhard metal borides, such as rhenium diboride (ReB_2).[4–7]

The design rules that led to the discovery of WB_4 and ReB_2 were inspired by considering how diamond, the hardest natural material in the world, achieves its unique mechanical properties.[8] The phenomenal hardness of diamond (70-110 GPa)[9] can be attributed to the three-dimensional network of

strong, short covalent bonds formed by carbon atoms, which helps resist the motion of dislocations and results in a high shear modulus. The excellent incompressibility (bulk modulus = 442 GPa),[10] on the other hand, results from its high valence electron density (0.705 electrons/Å^3), which is believed to be the determining factor for bulk modulus. Therefore, it was reasoned that superhard compounds could be obtained by combining elements that are capable of forming short covalent bonds such as boron and elements with high valence electron density such as tungsten or rhenium. Indeed, a new superhard material, hafnium/yttrium dodecaboride[11] ($Hf_{1-x}Y_xB_{12}$), was recently produced following this design rule. One challenge with these materials, however, is the need for excess boron to thermodynamically drive the formation of higher boride over the kinetically more favorable lower borides. For example, WB_4 can only be made by arc melting with a W:B molar ratio of ~1:12,[12] and YB_{12} requires a ratio of 1:20. Removing the excess boron is still a major challenge, resulting in sample nonuniformity.[13,14]

In contrast to higher borides, lower borides, for example, tungsten monoboride (WB), can be made at an exact W:B molar ratio of 1:1 without any stoichiometric issues. WB crystallizes in either a tetragonal phase at low temperature (LT) or an orthorhombic phase at high temperature (HT) with a transition temperature of 2170 °C (Fig. S1 in the supplementary material).[15] The HT-WB phase can be stabilized at room temperature with the addition of small amounts of Ta (1%–5%). Synchrotron-based high pressure studies show that the LT-WB is less compressible, while the stabilized HT-WB supports a higher differential strain and shows a higher onset of plastic deformation.[16] It is not surprising that neither phase is superhard based on microindentation hardness tests (35.5 ± 2.5 GPa for HT-WB, 31 ± 3.0 GPa for LT-WB) because of the significantly reduced level of covalent B–B bonding in these materials. Yeung *et al.*[17] have demonstrated, however, that the hardness of WB can be improved with the addition of Ta, resulting in a distortion of the tetragonal host matrix crystal structure into an orthorhombic structure. The hardness of three $Ta_xW_{1-x}B$ solid solution samples containing 5%, 25%, and 50% Ta is summarized in Table S1 in the supplementary material showing that a maximum value of 42.8 ± 2.6 GPa at 50 at. % Ta. Although the hardness under varied applied loads has been studied, the dopant concentration induced change in their elastic deformation behavior such as incompressibility and crystal lattice strain is still unknown. In addition, Vickers hardness tests cannot provide lattice specific information about hardness, which is the key to understanding the mechanisms for increasing the hardness of $Ta_xW_{1-x}B$ solid solutions.

Here, we performed synchrotron-based angle dispersive X-ray diffraction (XRD) experiments in radial geometry[18–23] using a diamond anvil cell (DAC)[24] to evaluate the bulk modulus and anisotropic lattice strain deformation behavior in this family of $Ta_xW_{1-x}B$ solid solutions. The non-hydrostatic high-pressure diffraction experiments can provide valuable insights for understanding the hardening mechanisms in these solid solutions, showing which lattice planes are most affected by the addition of Ta. It can also help separate intrinsic hardening effects from extrinsic ones.[25]

EXPERIMENTAL PROCEDURE

Three solid solutions of $Ta_xW_{1-x}B$ with x = 0.05, 0.25, and 0.50 were synthesized by arc melting. The powder of tungsten (99.95%, Strem Chemicals, USA), tantalum (Roc/Ric, 99.9%), and amorphous boron (99+%, Strem Chemicals, USA) were weighed according to the composition of each sample. Powders were then mixed together thoroughly in an agate mortar using a pestle followed by pressing into pellets under an applied load of 10 tons using a hydraulic Carver press. Subsequently, the pellets were placed in an arc-melting furnace filled with high-purity argon and a ~100 A DC current was applied for 1–2 min to arc-melt the samples. In order to ensure homogeneity, the fused ingots were then flipped over and re-arced. The ingots were then crushed and ground to fine powders with a particle size of <20 μm.

The *in situ* angle-dispersive high pressure radial X-ray diffraction experiments were performed at the Advanced Light Source (ALS) at Lawrence Berkeley National Laboratory (LBNL) on synchrotron beamline 12.2.2 in order to study the lattice-plane deformation behavior of $Ta_xW_{1-x}B$ solid solutions subjected to a large applied non-hydrostatic stress. The sample was loaded into the hole (~50 μm in diameter) of a boron-epoxy gasket (~400 μm in diameter and ~60 μm in thickness) in a diamond (~300 μm in culet size) anvil cell (DAC) without a pressure-transmitting medium in order to maximize the non-hydrostatic stress components. Each sample was loaded in the same way, in three separate DACs. A small piece of Pt foil (~20 μm in diameter) was placed on the top of the sample to serve as a pressure calibrant. The incident monochromatic X-ray with a wavelength of 0.4959 Å was collimated to 20 × 20 μm in beam size and then passed through the sample parallel to the diamond culet. The pressure was increased in ~4 GPa steps and the 2D diffraction image was collected with program FIT2D[26] after calibration of the detector distance and orientation using a LaB_6 standard.

The polycrystalline sample undergoes considerable deformation in the DAC as compression increases. The state of stress and d spacings of sample were analyzed using lattice strain theory.[27–29] A compressed sample under uniaxial loading in a DAC is subjected to a macroscopic differential stress, t, which is limited by the shear strength, τ, and the yield strength, σ_y, according to the Tresca yield criterion[30]

$$t = \sigma_3 - \sigma_1 \leq 2\tau = \sigma_y. \quad (1)$$

Here, σ_3 is the maximum stress along the compression direction, and σ_1 is the minimum stress parallel to the diamond culet. By examining the macroscopic differential stress, one can evaluate the lower-bound of the material's yield strength. The relationship between the measured *d-spacing*, $d_m(hkl)$, and φ, the angle between the diffracting plane normal and the loading axis, is given by

$$d_m(hkl) = d_p(hkl)[1 + (1 - 3\cos^2\varphi)Q(hkl)], \quad (2)$$

where $d_p(hkl)$ is the d spacing resulting from the hydrostatic component of stress, Q(hkl), which is the orientation dependent lattice strain,[31] which can be written as

$$Q(hkl) = \left(\frac{t}{3}\right)\{\alpha[2G_R(hkl)]^{-1} + (1-\alpha)(2G_V)^{-1}\}. \quad (3)$$

Here, $G_R(hkl)$ is the lattice dependent Reuss shear modulus under an iso-stress[32] condition, while G_V is the lattice independent Voigt shear modulus under an iso-strain[33] condition. Note that most high pressure studies, especially for superhard materials, use the iso-stress assumption.[25,34] The differential stress supported by a set of lattice planes (hkl) can be estimated using the relation[35,36]

$$t = 6G(hkl)\langle Q(hkl)\rangle. \quad (4)$$

The $\langle Q(hkl)\rangle$ can be resolved from the ratio of the slope to the intercept in the plot of $d_m(hkl)$ vs $(1-3\cos^2\varphi)$ according to Eq. (2) and it is believed to be a good qualitative indicator of hardness since Q(hkl) reflects the contributions of both plastic and elastic deformation.[37,38] The $d_p(hkl)$ measured at $\varphi = 54.7°$ reflects the compression behavior due to hydrostatic component of stress. In other words, the equivalent hydrostatic compression curve can be derived from non-hydrostatic data. The ambient bulk modulus, K_0, then can be determined by fitting the compression curve to the second order Birch-Murnaghan equation-of-state (EOS)[39]

$$P = 1.5\ K_0\ [(V/V_0)^{-7/3} - (V/V_0)^{-5/3}]. \quad (5)$$

Note that the unit cell volume at each pressure is measured at $\varphi = 54.7°$.

RESULTS AND DISCUSSION

$Ta_{0.05}W_{0.95}B$, $Ta_{0.25}W_{0.75}B$, and $Ta_{0.50}W_{0.50}B$ solid solutions were individually compressed non-hydrostatically in a DAC up to 52 GPa, 51 GPa, and 65 GPa. Note that the diffraction patterns were collected at steps of ~4 GPa and the pressure was determined at $\varphi = 54.7°$ by fitting the equation-of-state of Pt[40] to its unit cell volume. As can been seen in the two-dimensional image (Fig. 1), the diffraction peaks shift toward higher diffraction angles with increased pressure. Greater shifts are found in the high stress direction indicated with an arrow. The change from circular to elliptic diffraction rings is a result of differential stress, which is believed to be related to the elastic limit of the sample. Note that the spotty pattern, which arises because of the finite number of grains in the sample volume, prevents texture analysis. Examples of full integrated low and high pressure one-dimensional diffraction pattern of $Ta_xW_{1-x}B$ solid solutions are shown in Fig. S2 in the supplementary material. The stick reference pattern given below the experimental diffraction peaks is from the Joint Committee on Powder Diffraction Standards (JCPDS Card #00-006-0541). As can be seen in the figure, all three WB solid solutions containing Ta crystallize in the orthorhombic HT structure. A clear shift toward lower angle is observed with increasing Ta content because the atomic size of Ta (1.49 Å) is larger than that of W (1.41 Å).[41] Shifts to higher angle are observed at higher pressure.

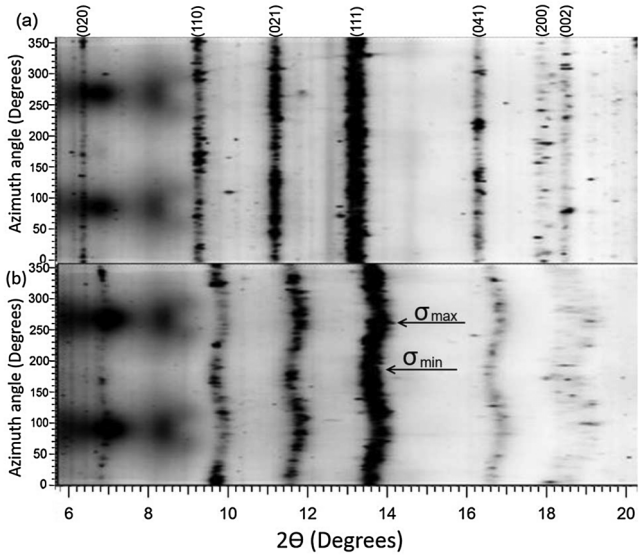

FIG. 1. Representative 2D caked image pattern of $Ta_{0.50}W_{0.50}B$ collected at (a) ambient pressure and (b) 42.4 GPa, plotted as a function of azimuth angle and diffraction angle.

The pressure dependence of the lattice constants for $Ta_xW_{1-x}B$ solid solutions is summarized in Fig. 2 and Table S2

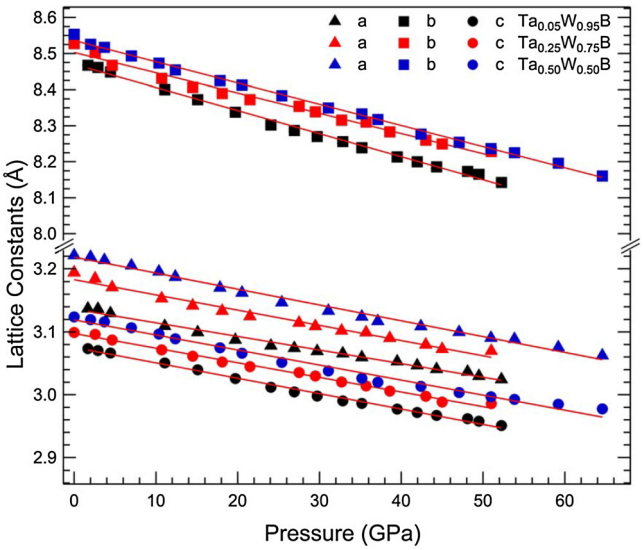

FIG. 2. Measured lattice constants collected at $\varphi = 54.7°$ for all three WB solid solutions as a function of pressure. Error bars that are smaller than the size of the symbol have been omitted.

in the supplementary material. There are no signs of phase transformations upon compression. In addition, since TaB is fully miscible with WB, no pure metals or any other secondary phases are found in the diffraction pattern across the entire pressure range, suggesting that extrinsic hardening mechanisms[2,42] such as precipitation hardening or dispersion hardening are not responsible for the observed increase in hardness (Table S1 in the supplementary material). The hardness enhancement in $Ta_xW_{1-x}B$ solid solutions can thus be attributed to solid solution hardening driven either by the atomic size mismatch between Ta and W, or by some electronic structure change resulting from incorporation of elements of different valence electron count.

To obtain the differential strain, peak positions as a function of the angle φ were fit according to Eq. (2). An example of such fits with excellent linearity is shown in Fig. S3 in the supplementary material for the (200), (020), and (002) lattice planes of $Ta_{0.50}W_{0.50}B$ at a pressure of 42.4 GPa. This study focuses on the role of metal composition in determining the directional-dependent mechanical properties. The three orthogonal planes were therefore chosen because they reflect the anisotropic deformation behavior of the lattice constants *a*, *b*, and *c* in the orthorhombic structure. The intercept of each line gives the *d-spacing* under the hydrostatic equivalent stress, while the slope yields the lattice strain. Because the shear modulus is not known for these solid solutions, those data are left as the ratio of the differential stress to the aggregate shear modulus (t(hkl)/G), which is equivalent to the differential strain. These *t*/G values for $Ta_{0.05}W_{0.95}B$ (black), $Ta_{0.25}W_{0.75}B$ (red), and $Ta_{0.50}W_{0.50}B$ (blue) are plotted as a function of pressure in Fig. 3. Although the shear moduli across solid solutions were not measured, their variations with metal composition are believed to be modest.[43] Therefore, the general trends in t(hkl)/G can be considered as good qualitative indicators of trends in *t*(*hkl*).

Figure 3(a) shows data for t(020)/G ratio for the three samples. The trends are very similar in all cases, with the ratio initially increasing linearly with pressure, then leveling off between 20 and 30 GPa, and increasing much more slowly afterwards, ending with a plateau, which can be explained as the onset of plastic deformation or yield by a slip system.[37] When the concentration of Ta is first increased from 5% to 25%, no clear change in the plateau value is observed. If we interpret the extent of supported differential strain as a yield strength estimate, this suggests that at low doping level, the hardness enhancement is not due to the strengthening of the [020] direction, i.e., the *b*-axis. However, when 50% Ta is substituted for W, the t(020)/G ratio increased from 4.6% to 5.2% at the highest value, suggesting that strengthening of the *b*-axis by solid solution hardening becomes more important at higher doping levels.

As can be seen in Fig. 3(b), the (002) plane supports a lower differential strain compared to the (200) and (002) planes. This may indicate that the [002] or *c*-axis is the weakest direction. In addition, the t(002)/G of $Ta_{0.05}W_{0.95}B$ shows a plateau indicative of plastic deformation in the 20-40

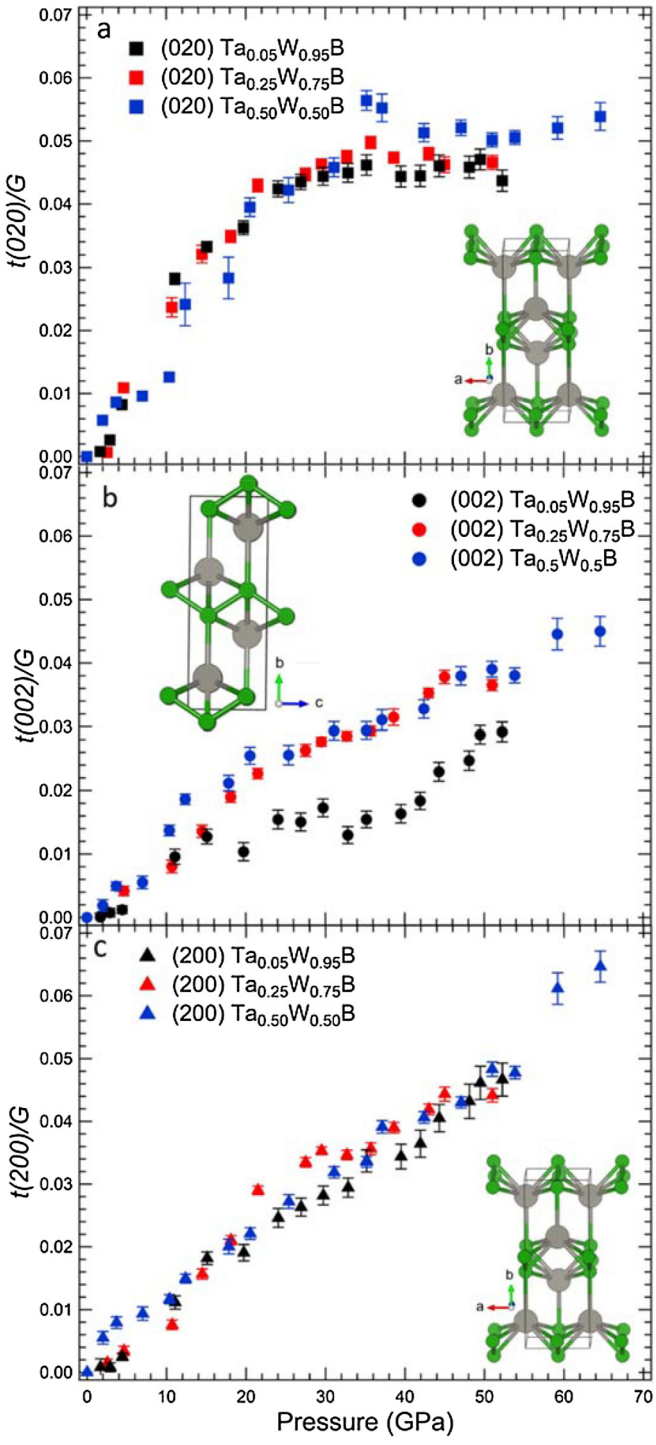

FIG. 3. Evolution of the differential strain in each lattice direction for WB solid solutions with Ta concentrations of 5%, 25%, and 50%. Panels are: (a) *t*(*020*)/*G*, (b) *t*(*002*)/*G*, and (c) *t*(*200*)/*G*. The insets show the crystal structure of the orthorhombic WB, with the boron atoms in green and tungsten atoms in gray.

GPa range with a t/G value of 1.5%, but at higher pressures, it resumes increasing. This high pressure increase in differential strain may result from work hardening effects, which are not found in either $Ta_{0.25}W_{0.75}B$ or $Ta_{0.50}W_{0.50}B$. When the Ta concentration is increased from 5% to 25%, a clear increase in the $t(002)/G$ ratio is observed, and the low pressure plateau disappears, suggesting that solid solution effects may be preventing slip in this direction. However, with a further increase in concentration to 50%, there is no additional change in $t(002)/G$. This behavior suggests that strengthening of the (002) plane produces large changes at low concentration of heteroatoms, but that the effect saturates at higher solid solution fractions.

Unlike the (020) and (002) planes, the trend in the (200) plane shows no plateau across the entire pressure range, indicating that the a-axis has not yielded by the highest pressure reached in this experiment [65 GPa, Fig. 3(c)]. Given that the (200) supports the highest t/G ratio among the three selected planes for all solid solutions, the [200] or a-axis direction appears to be the hardest direction.

One can gain some insights into the strength anisotropy by considering the structure of WB. As shown in the inset, the a-axis is dominated by strong W–B bonds, which are believed to be the cornerstone of the materials strength for monoborides,[44] while the b- and c-directions involve fewer W–B bonds. In addition, the $t(200)/G$ ratio of the three solid solutions presents nearly the same linear relationship with pressure, regardless of the dopant concentration, indicating that solid solution hardening is not pronounced along the a-axis. In other words, the intrinsically hardest direction cannot be further strengthened by solid solution hardening. Therefore, despite the fact that $Ta_{0.50}W_{0.50}B$ (and all the other compositions) reach a maximum in $t(200)/G$ with a value of 6.5% at 65 GPa, this plane does not slip at any modest pressures and so is not important for controlling material failure.

Because of the highly anisotropic nature of this orthorhombic lattice, it is useful to examine the b/a ratio of WB solid solutions as a function of orientation ($\varphi = 0°$, 54.7°, and 90°) as another way to visualize the onset of plastic deformation. In a radial diamond anvil cell, whenever a crystallite of orthorhombic $Ta_xW_{1-x}B$ is oriented with its b-axis along the maximum stress direction ($\varphi = 0°$), it will have its a-axis and c-axis oriented along the two minimum stress directions ($\varphi = 90°$). Therefore, a lattice b value measured in the high stress direction is always paired with a lattice a value in the low stress direction and vice versa. Paired b/a ratios can thus be calculated at $\varphi = 0°$, 90°, and under isotropic conditions at 54.7°. In these data, a clear discontinuous change in b/a ratio for the three solid solutions is observed in all orientations (Fig. 4). This discontinuity can be associated with the onset of plastic deformation and thus a deviation from linear compressibility. In agreement with the trends in hardness, this onset value is observed to increase from ~15 GPa for the 5% Ta sample to 20–25 GPa for the 25% Ta sample to greater than 30 GPa for the 50% Ta sample.

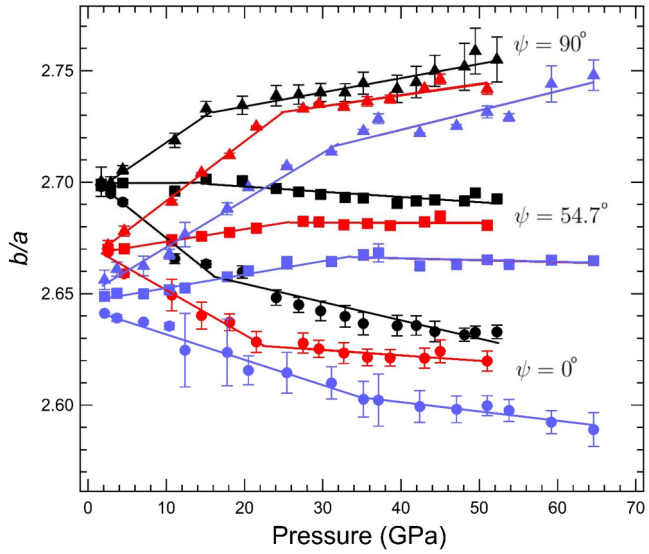

FIG. 4. Orientation dependence of b/a for $Ta_xW_{1-x}B$ solid solutions as a function of pressure. The labeled angle corresponds to the b-axis value used in the calculations. $Ta_{0.05}W_{0.95}B$, $Ta_{0.25}W_{0.75}B$, and $Ta_{0.50}W_{0.50}B$ are in black, red, and blue, respectively. A discontinuous change in slope is observed for all samples, and the pressure of the discontinuity increases with increasing Ta content.

In addition to trends in the t/G ratio, we also examined trends in bulk modulus across the solid solution samples. The incompressibility was determined by fitting both second-order and third-order Birch–Murnaghan equations-of-state to the unit cell volume as a function of pressure as shown in Fig. 5, and Figs. S4 and S5 in the supplementary material. We note that the data collected at low pressures in radial diffraction (non-hydrostatic compression) tend to show a higher uncertainty because at low pressures the sample is not compact enough, leading to a nonuniform stress state. The bulk modulus values for $Ta_{0.05}W_{0.95}B$, $Ta_{0.25}W_{0.75}B$, and $Ta_{0.50}W_{0.50}B$ are 341 ± 5, 340 ± 6, and 337 ± 3 GPa, respectively, which are all the same within experimental error. The values from third order fitting are 329 ± 8, 327 ± 14, and 345 ± 5 GPa with pressure derivative values of 4.6, 5.2, and 3.3. These values are again similar, and the slightly larger variation likely stems from variation in the derivative values, which are hard to fit accurately. This result is somewhat surprising, given the bulk modulus of TaB (277 GPa),[45] which is much lower than WB (351 GPa).[46] Note that the TaB theoretical values were calculated based on the generalized gradient approximation (GGA). The authors also presented a bulk modulus value of 302 GPa for TaB, which is an average of the GGA and LDA values and they believe it is more accurate. For many solid solutions, the bulk moduli are just linear combinations of the two end members, as found in $Os_{1-x}Ru_xB_2$ solid solutions.[47] This divergence from Vegard's Law may arise from the fact that tantalum is only one atomic number less than tungsten, and so they have the same core electron count, which is

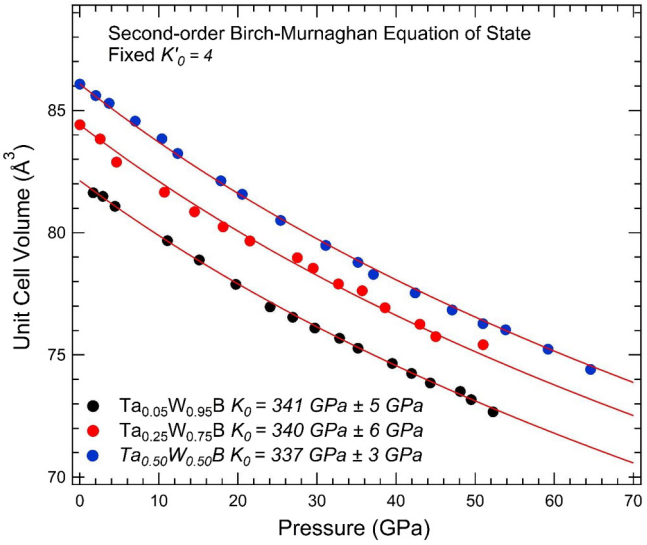

FIG. 5. Pressure dependence of unit cell volume for WB solid solutions under non-hydrostatic compression. The volume data were collected at $\varphi = 54.7°$. The solid line in the plot is the best fit of the second-order Birch–Murnaghan equation of state to the compression data. All values are essentially the same within experimental error.

believed to play an important role in determining bulk modulus, in addition to the valence electron count.

CONCLUSIONS

We have compared the differential strain supported by $Ta_xW_{1-x}B$ solid solutions across compositions to understand hardness enhancements in a lattice specific manner. When the concentration of Ta is increased from 5% to 25%, plastic deformation in the (002) direction, which is the weakest direction, is suppressed by solid solution hardening, indicating that strengthening of the (002) direction is responsible for the hardness enhancement observed in going from $Ta_{0.05}W_{0.95}B$ to $Ta_{0.25}W_{0.75}B$. With further addition of Ta up to 50%, there is no further increase in the t(002)/G ratio; however, there is a slight increase in the plateau value of t(020)/G at this highest Ta ratio, suggesting that strengthening of the *b*-axis may be responsible for the hardness increase observed on going from $Ta_{0.25}W_{0.75}B$ to $Ta_{0.50}W_{0.50}B$. No solid solution hardening is found in the [200] direction, regardless of the dopant concentration. The *a*-axis, i.e., the hardest direction, thus appears to provide little contribution to the hardness enhancement in $Ta_xW_{1-x}B$ solid solutions. Calculated values of the b/a ratio allow us to visualize how the onset of plastic deformation increases with increasing Ta content. Finally, examination of the bulk modulus across compositions shows that they all have remarkably similar values, indicating that changes in bulk modulus do not contribute to changes in hardness.

SUPPLEMENTARY MATERIAL

See supplementary material for additional characterization of the $Ta_xW_{1-x}B$ solid solutions. The data include hardness as a function of load, diffraction peaks positions as a function of pressure, cartoons of relevant crystal structures, examples of high pressure diffraction patterns and their analysis, and equation of state calculations.

ACKNOWLEDGMENTS

The authors thank M. Kunz and A. MacDowell for technical support at the Lawrence Berkeley National Laboratory (LBNL) beamline 12.2.2. We also thank Professor H.-R. Wenk for equipment support. This work was funded by the National Science Foundation (NSF) under Grant No. DMR-1506860 (S.H.T. and R.B.K.). Radial diffraction experiments were performed at the Advanced Light Source 12.2.2 (LBNL). The Advanced Light Source is supported by the Director, Office of Science, Office of Basic Energy Sciences, of the U.S. Department of Energy under Contract No. DE-AC02-05CH11231. This research was partially supported by COMPRES, the Consortium for Materials Properties Research in Earth Sciences under NSF Cooperative Agreement EAR 1606856.

REFERENCES

[1]R. Mohammadi, A. T. Lech, M. Xie, B. E. Weaver, M. T. Yeung, S. H. Tolbert, and R. B. Kaner, Proc. Natl. Acad. Sci. U.S.A. **108**, 10958 (2011).
[2]R. Mohammadi, M. Xie, A. T. Lech, C. L. Turner, A. Kavner, S. H. Tolbert, and R. B. Kaner, J. Am. Chem. Soc. **134**, 20660 (2012).
[3]M. Xie, R. Mohammadi, Z. Mao, M. M. Armentrout, A. Kavner, R. B. Kaner, and S. H. Tolbert, Phys. Rev. B **85**, 064118 (2012).
[4]A. Kavner, M. B. Weinberger, R. B. Kaner, and S. H. Tolbert, J. Appl. Phys. **112**, 013526 (2012).
[5]H.-Y. Chung, M. B. Weinberger, J. B. Levine, A. Kavner, J.-M. Yang, S. H. Tolbert, and R. B. Kaner, Science **316**, 436 (2007).
[6]T. Taniguchi, M. Akaishi, and S. Yamaoka, J. Am. Ceram. Soc. **79**, 547 (1996).
[7]A. T. Lech, C. L. Turner, J. Lei, R. Mohammadi, S. H. Tolbert, and R. B. Kaner, J. Am. Chem. Soc. **138**, 14398 (2016).
[8]M. T. Yeung, R. Mohammadi, and R. B. Kaner, Annu. Rev. Mater. Res. **46**, 465 (2016).
[9]M. L. Cohen, Science **261**, 307 (1993).
[10]I. Aleksandrov, A. Goncharov, A. Zisman, and S. Stishov, Sov. Phys. JETP **66**, 384 (1987).
[11]G. Akopov, M. T. Yeung, C. L. Turner, R. L. Li, and R. B. Kaner, Inorg. Chem. **55**, 5051 (2016).
[12]P. A. Romans and M. P. Krug, Acta Crystallogr. **20**, 313 (1966).
[13]R. Mohammadi, C. L. Turner, M. Xie, M. T. Yeung, A. T. Lech, S. H. Tolbert, and R. B. Kaner, Chem. Mater. **28**, 632 (2016).
[14]A. T. Lech, S. H. Tolbert, R. B. Kaner *et al.*, Proc. Natl. Acad. Sci. U.S.A. **112**, 3223 (2015).
[15]H. Duschanek and P. Rogl, J. Phase Equilib. **16**, 150 (1995).
[16]J. Lei, M. T. Yeung, P. J. Robinson, R. Mohammadi, C. L. Turner, J. Yan, A. Kavner, A. N. Alexandrova, R. B. Kaner, and S. H. Tolbert, J. Phys. Chem. C **122**, 5647 (2018).
[17]M. T. Yeung, J. Lei, R. Mohammadi, Y. Wang, S. H. Tolbert, and R. B. Kaner, Adv. Mater. **28**, 6993 (2016).
[18]H. K. Mao, J. F. Shu, G. Y. Shen, R. J. Hemley, B. S. Li, and A. K. Singh, Nature **396**, 741 (1998).
[19]S. Merkel, J. Phys. Condens. Matter **18**, 949 (2006).
[20]T. S. Duffy, AIP Conf. Proc. **955**, 639 (2007).

[21]B. Chen, K. Lutker, S. V. Raju, J. Yan, W. Kanitpanyacharoen, J. Lei, S. Yang, H.-R. Wenk, H.-K. Mao, and Q. Williams, Science **338**, 1448 (2012).
[22]B. Chen, K. Lutker, J. Lei, J. Yan, S. Yang, and H. Mao, Proc. Natl. Acad. Sci. U.S.A. **111**, 3350 (2014).
[23]X. Zhou, N. Tamura, Z. Mi, J. Lei, J. Yan, L. Zhang, W. Deng, F. Ke, B. Yue, and B. Chen, Phys. Rev. Lett. **118**, 096101 (2017).
[24]R. J. Hemley, H. K. Mao, G. Shen, J. Badro, P. Gillet, M. Hanfland, and D. Häusermann, Science **276**, 1242 (1997).
[25]M. Xie, R. Mohammadi, C. L. Turner, R. B. Kaner, A. Kavner, and S. H. Tolbert, Appl. Phys. Lett. **107**, 041903 (2015).
[26]A. P. Hammersley, S. O. Svensson, M. Hanfland, A. N. Fitch, and D. Hausermann, High Press. Res. **14**, 235 (1996).
[27]A. K. Singh, H.-K. Mao, J. Shu, and R. J. Hemley, Phys. Rev. Lett. **80**, 2157 (1998).
[28]A. K. Singh, J. Appl. Phys. **73**, 4278 (1993).
[29]A. K. Singh, C. Balasingh, H.-K. Mao, R. J. Hemley, and J. Shu, J. Appl. Phys. **83**, 7567 (1998).
[30]A. L. Ruoff, J. Appl. Phys. **46**, 1389 (1975).
[31]A. K. Singh, J. Appl. Phys. **106**, 043514 (2009).
[32]A. Reuss, Z. Angew. Math. Mech. **9**, 49 (1929).
[33]W. Voigt, *Lehrbuch der Kristallphysik* (Teubner, Leipzig, 1928).
[34]M. Xie, R. Mohammadi, C. L. Turner, R. B. Kaner, A. Kavner, and S. H. Tolbert, Phys. Rev. B **90**, 104104 (2014).
[35]Y. B. Wang, T. Uchida, R. Von Dreele, M. L. Rivers, N. Nishiyama, K. Funakoshi, A. Nozawa, and H. Kaneko, J. Appl. Crystallogr. **37**, 947 (2004).
[36]T. Uchida, Y. B. Wang, M. L. Rivers, and S. R. Sutton, Earth Planet. Sci. Lett. **226**, 117 (2004).
[37]G. M. Amulele, M. H. Manghnani, and M. Somayazulu, J. Appl. Phys. **99**, 023522 (2006).
[38]D. W. He, S. R. Shieh, and T. S. Duffy, Phys. Rev. B **70**, 184121 (2004).
[39]F. Birch, J. Geophys. Res. **83**, 1257 (1978).
[40]Y. Fei, A. Ricolleau, M. Frank, K. Mibe, G. Shen, and V. Prakapenka, Proc. Natl. Acad. Sci. U.S.A. **104**, 9182 (2007).
[41]T. Egami and Y. Waseda, J. Non-Cryst. Solids **64**, 113 (1984).
[42]S. Veprek, J. Vac. Sci. Technol. A **17**, 2401 (1999).
[43]M. B. Kanoun, P. Hermet, and S. Goumri-Said, J. Phys. Chem. C **116**, 11746 (2012).
[44]L. Han, S. Wa, C. Jin *et al.*, Appl. Phys. Lett. **106**, 221902 (2015).
[45]H.-H. Chen, Y. Bi, Y. Cheng, G. Ji, and L. Cai, J. Phys. Chem. Solids **73**, 1197 (2012).
[46]X.-Y. Cheng, X.-Q. Chen, D.-Z. Li, and Y.-Y. Li, Acta Crystallogr. **70**, 85 (2014).
[47]M. B. Weinberger J. B. Levine *et al.*, Chem. Mater. **21**, 1915 (2009).